Reexamining the potential to classify lava flows from the fractality of their margins

E. I. Schaefer[1], C. W. Hamilton[2], and C. D. Neish[3]

[1] Department of Earth Sciences, University of Western Ontario, 1151 Richmond Street N., London, Ontario, N6A 5B7 Canada

[2] Institute for Earth and Space Exploration, University of Western Ontario, 1151 Richmond Street N., London, Ontario, N6A 5B7 Canada

[3] Lunar and Planetary Laboratory, University of Arizona, 1629 E. University Blvd., Tucson, Arizona, 85721 USA

Corresponding author: Ethan I. Schaefer (ethan.i.schaefer@gmail.com)

Key Points:

- The fractality of lava flow margins is highly diverse and shows varying scale dependence, even among flows of the same morphologic type.
- Topographic confinement and substrate slopes can modify the fractaliy of a lava flow's margin without imparting a recognizable signature.
- These complexities preclude robust, unique identification of a lava flow's morphologic type from the meter-scale fractality of its margin.

Abstract

Can fractal analysis enable us to classify a lava flow to a morphologic type (e.g., ʻaʻā vs. pāhoehoe) solely by examining the geometry of the flow's margin? If so, these classifications would provide insights into the rheology and dynamics of the flow when it was emplaced. Furthermore, the potential to classify lava flows from remotely-sensed data would particularly benefit the analysis of flows for which field access is not feasible. The technique's current framework depends on three assumptions: (1) measured lava margin fractality is scale-invariant; (2) different morphologic types are consistently distinguishable based on their measured fractality; and (3) any modification of margin fractality by substrate slope or topographic confinement would be minimal or have a recognizable signature. In this study, we critically evaluate each of these assumptions at meter scales using 15 field-collected margin intervals from a wide variety of morphologic types in Hawaiʻi, Iceland, and Idaho. Among the 12 margin intervals that satisfy the current framework's expectations, 5 exhibit notably scale-dependent fractality and all 5 from transitional lava types would be classified as ʻaʻā or pāhoehoe at some scales. Additionally, an ʻaʻā flow on a 15° slope (Mauna Ulu, Hawaiʻi) and a spiny pāhoehoe flow confined by a stream bank (Holuhraun, Iceland) exhibit significantly depressed fractalities but lack distinctive signatures for these modifications. We therefore conclude that all three assumptions are invalid at meter scales. Although fractal analysis of lava margins can provide some constraints on morphologic type, unique classification is not robust at these scales.

1 Introduction

Fractal analysis provides an elegant way to succinctly describe the complex geometries of lava margins. It may also hold substantial promise to constrain the rheology, emplacement dynamics, and chemical composition of flows. Bruno et al. (1992) and Gaonac'h et al. (1992) were the first to demonstrate that the geometry of lava flow margins is empirically fractal. That is, the apparent length of these margins, when measured at progressively coarser resolutions, approximately decreases by a power-law over some range of scales. Because fractal geometries naturally arise from nonlinear processes, the fractal analysis of lava margins was expected to provide direct insights into the fluid dynamics of lava flows (e.g., Bruno et al., 1992, 1994; Gaonac'h et al., 1992; C. R. J. Kilburn, 1996). Moreover, Bruno et al. (1992, 1994) and Gaonac'h et al. (1992) presented evidence that the empirical fractality of lava margins might extend from decimeter to kilometer scales, and Bruno et al. (1992, 1994) demonstrated that this fractality could help to discriminate between two morphologic lava types: ʻaʻā and pāhoehoe. Knowledge of a flow's morphologic type can, in turn, help to constrain the dynamics, rheology, effusion rate, and crustal disruption history of the lava at the time of its emplacement (e.g., Cashman et al., 1999; Hamilton, 2019; Peterson & Tilling, 1980; Rowland & Walker, 1990). In addition, Bruno et al. (1994) found that flows of intermediate to silicic composition had measured lengths that departed from power-law scaling, at least at scales of hundreds of meters, suggesting that fractal analysis of margin geometries could be used to distinguish mafic lavas from those with more evolved compositions.

Any insights provided by margin fractal analysis would especially facilitate the characterization of lava flows in remote areas. Although field observations provide better constraints (e.g., Harris et al., 2017; L Keszthelyi, 2002; Self et al., 1996; Thor Thordarson, 1995), such ground-truthing is not feasible for many flows. For that reason, researchers have used margin fractal analysis to investigate submarine lava flows on Earth (Maeno et al., 2016;

Mitchell et al., 2008; Wroblewski et al., 2019) and flows of lava and impact melt on Mars, Venus, and Earth's moon (Bray et al., 2018; Bruno et al., 1992, 1994; Bruno & Taylor, 1995; Wroblewski et al., 2019; You et al., 1996).

The prevailing classification framework for the fractal analysis of mafic lava margins, due to Bruno et al. (1994), depends explicitly on three assumptions: (1) The measured fractality of a margin interval does not critically depend on the scale range over which that fractality is measured. (2) The measured margin fractalities of ʻaʻā, pāhoehoe, and so-called transitional lava types are each distinct. (3) The effects of topography, including sloped substrates and confinement, typically render a margin empirically non-fractal rather than merely modulate its empirical fractality. Where this framework is used to classify flows remotely, the results may depend critically on these assumptions. We therefore test each of these assumptions at meter scales using 15 field-collected margin intervals from a wide variety of morphologic types in Hawaiʻi, Iceland, and Idaho (Figure 1).

We first review the relevant background (section 2) that motivates us to test the assumptions enumerated above. We then explain how we interpret and quantify fractality in this study, including some methodological refinements to the fractal analysis of lava margins (section 3). We present our results (section 4) and then discuss how these results affect the interpretation of morphologic type from margin fractal analysis, especially where complementary data are limited (section 5). Finally, we summarize our principal conclusions (section 6).

2 Motivation

2.1 Scale dependence

The fractal analysis of topographic contours, including coastlines, provides a cautionary parallel to the fractal analysis of lava margins. The effective fractal dimension D (section 3.2.2) quantifies the fractality of natural geometries, and the D of topographic contours was long thought to be scale-invariant (B. Mandelbrot, 1967; Richardson, 1961). However, later work showed that these contours had distinctly different D values when measured over discrete scale ranges (Mark & Aronson, 1984). Still later, Andrle (1992, 1996b, 1996a) presented evidence that coastlines' D values vary continuously with scale, including the west coast of Britain, which is the archetypal natural fractal (B. Mandelbrot, 1967; Richardson, 1961).

The lava margin fractal analyses of Bruno et al. (1994) spanned scales of 0.125–2400 m and were split between 17 photographic analyses at scales of 12–2400 m and 27 field analyses at scales of 0.125–16 m. D measures scaling behavior, and therefore each measurement of D must be made over a range of scales, which we call a rod set (see section 4.2.2). Bruno et al. (1994) did not specify the rod set used in each measurement, but they did provide some generalities. In all field analyses, they used only one rod set (and therefore calculated exactly one D) per margin interval. Moreover, each rod set used in field analysis was selected from a collection of rods with lengths 0.125 m, 0.25 m, 0.5 m, 1 m, 2 m, 4 m, 8 m, and 16 m. Wherever possible, they specifically used a rod set of either 1–16 m or 0.5–16 m (corresponding to representative scales of $r^* = 4$ m and $r^* = 2.83$ m, respectively; see section 3.2.4). For shorter margin intervals, they used rods as short as 0.125 m ($r^* \geq 0.5$ m). Their use of only one rod set per field-analyzed margin interval and the preferential use of similar rod sets in field analyses could potentially mask any scale-dependent fractality at meter scales (see also section 5.2.1), which are the focus of the present study.

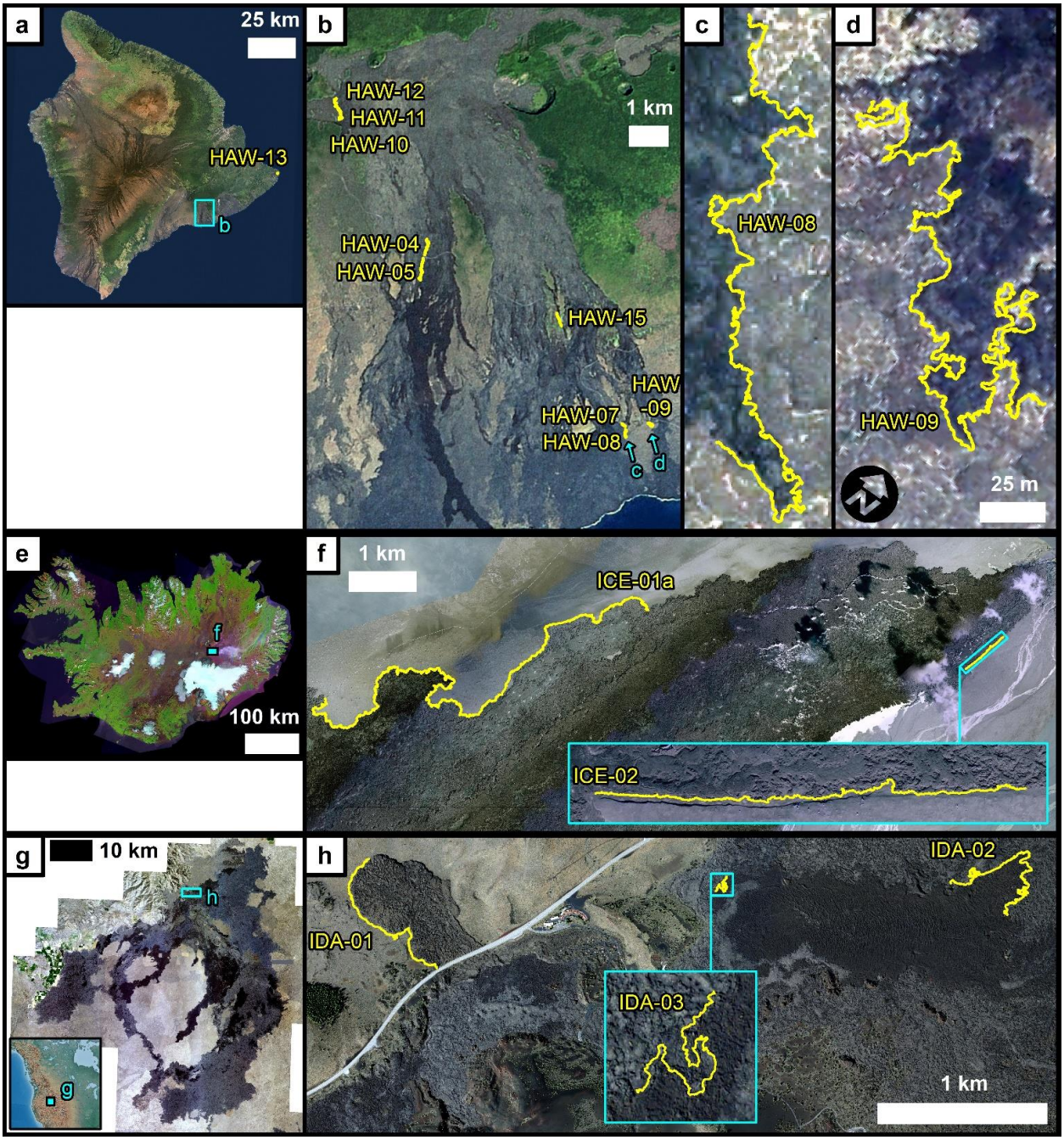

Figure 1. Locations of all 15 margin intervals (yellow lines) analyzed in the present study. (a) The island of Hawai‘i. (b) Study area in Hawai‘i Volcanoes National Park. (c)–(d): Magnified views of two margin intervals from (b). (e) Iceland. (f) Two margin intervals from the 2014–2015 Holuhraun flow field. (g) Study area and (h) margin intervals in Craters of the Moon National Monument and Preserve, Idaho, USA. Inset in (g) shows location in North America. Background of (a) and (b) is a Landsat 7 mosaic (15 m/pixel) created by Earthstar Geographics. Background of (c) and (d) is a QuickBird orthomosaic (0.6 m/pixel) from the Natural Resources Conservation Service of the United States Department of Agriculture. Background of (e) is a

Landsat 8 mosaic (66 m/pixel) created by the National Land Survey of Iceland. Background of (f) is a color orthoimage from Loftmyndir ehf. (0.5 m/pixel). Backgrounds of (g) and (h) are orthoimages (0.5 m/pixel) from the National Agriculture Imagery Program of the United States Department of Agriculture. Except for (d) and the inset in (f), north is up in all views.

In three cases, Bruno et al. (1994) also analyzed the same margin—albeit over different intervals—in paired field and photographic analyses. The measured disparities were similar to the single-rod-set along-length variabilities in D that they measured. They therefore interpreted D to be scale-invariant, but the limited scope of these paired analyses—three pāhoehoe margins, all from Hawai‘i, each analyzed with exactly two rod sets—may not be sufficient to characterize the frequency of scale-dependent fractality across morphologic types and geologic settings, especially at meter scales.

When exploring scale dependence, we primarily focus on meter scales. These scales are best supported by our data and were the primary focus of Bruno et al. (1994), whose study is the most extensive investigation of lava margin fractality to date. The scale dependence of empirical lava margin fractality is also least constrained at these scales, as described earlier in this section. Furthermore, meter scales are relevant in both terrestrial and planetary contexts. These scales are resolvable on Mars by the High Resolution Imaging Science Experiment (HiRISE) on board the *Mars Reconnaissance Orbiter*, which has a minimum pixel scale of 25 cm (McEwen et al., 2007), and on Earth's moon by both the Narrow Angle Cameras on board the *Lunar Reconnaissance Orbiter*, which has a minimum pixel scale of 50 cm (Robinson et al., 2010), and the Orbiter High Resolution Camera on board *Chandrayaan-2*, which has a minimum pixel scale of 25 cm (Chowdhury et al., 2020). Notably, Bray et al. (2018) recently applied meter-scale margin fractal analysis to lunar features that may represent impact melt flows.

2.2 Morphologic lava types

Morphologic lava types are commonly classified in a three-part system of ‘a‘ā, pāhoehoe, and block lava (Harris et al., 2017; Macdonald, 1953). ‘A‘ā and pāhoehoe are most commonly associated with basalt, whereas block lavas typically are more silicic (Finch, 1933). Other mafic lavas that are neither ‘a‘ā nor pāhoehoe are conventionally called "transitional" (see section 3.2.2). We direct the reader to Harris et al. (2017), Gregg (2017), and Hamilton (2019) for detailed descriptions of these types. Although lava types are traditionally distinguished by sub-meter surface morphology, they can also be identified from interior structure (e.g., Harris et al., 2017; L Keszthelyi, 2002; Self et al., 1996; Thor Thordarson, 1995). We include examples of ‘a‘ā, pāhoehoe, and transitional lavas in the present study, as well as one example of lava that may be intermediate between block lava and ‘a‘ā (Table 1).

2.2.1 ‘A‘ā and pahoehoe

Whether basaltic lava freezes to form a crust of ‘a‘ā or pāhoehoe is determined by both the rheology and dynamics of the flow, with pāhoehoe favored by lower apparent viscosities and lower shear strain rates (Macdonald, 1953; Peterson & Tilling, 1980). These properties can be interpreted as lower yield strengths and lower rates of net crustal disruption, respectively (Cashman et al., 1999; Christopher R J Kilburn, 1990). A flow can also transition from pāhoehoe to ‘a‘ā (or, more rarely, from ‘a‘ā to pāhoehoe) as the apparent viscosity and shear strain rate change along the flow's path (Hon et al., 2003; Lipman & Banks, 1987; Macdonald, 1953;

Wolfe et al., 1988). For example, steep substrates can increase local flow velocities and hence shear strain rate, such that pāhoehoe transitions to ʻaʻā (e.g., Macdonald, 1953; Peterson & Tilling, 1980).

Bruno et al. (1994) primarily focused on margins of ʻaʻā and pāhoehoe. We therefore include nine margin intervals of ʻaʻā or pāhoehoe to facilitate comparison of our results to theirs.

2.2.2 Transitional lavas

The genetic interpretation of so-called "transitional" lavas is somewhat less resolved than that of ʻaʻā and pāhoehoe. Several workers have reported continuous and long-lived formation of transitional lavas at active flows (e.g., Lipman & Banks, 1987; Pedersen et al., 2017), whereas others have interpreted transitional lavas to form from episodic disruption of otherwise stable crusts (Hamilton, 2019; Laszlo Keszthelyi et al., 2004). Further research is necessary to clarify the origins of and relationships between transitional types (cf. Cashman et al., 1999; Hon et al., 2003; Christopher R J Kilburn, 1990; Peterson & Tilling, 1980; Soule & Cashman, 2005).

To reasonably classify lavas, one must consider transitional types in addition to the traditional ʻaʻā and pāhoehoe end-members. For example, pāhoehoe and rubbly lava are the dominant types in Iceland (T. Thordarson & Höskuldsson, 2008). Rubbly and slabby lavas may also be important on Mars, based on the observation of similar morphologies in terrestrial and Martian flow fields at scales of tens of meters or more (L. Keszthelyi et al., 2000; Laszlo Keszthelyi et al., 2004; Voigt & Hamilton, 2018). These observations motivate us to include transitional types in our analysis, especially as these types have not yet been a major focus of margin fractal analysis (cf. Bruno et al., 1994). Six of our margin intervals target one or more transitional types, and two of these intervals come from the outermost margin of the 2014–2015 Holuhraun eruption (Figure 1f), which was extensively studied while active (e.g., Kolzenburg et al., 2017; Pedersen et al., 2017). The level, easily traversable sand sheet adjacent to a portion of this margin enabled us to collect an uninterrupted interval nearly 19 km long (ICE-01a).

Note that HAW-13a (Figure S2) is unique in the present study as it is the only margin interval that delineates the boundary between two subtypes within the same flow. Namely, HAW-13a represents the edge of a subtype of spiny pāhoehoe that Rowland and Walker (1987) called "primary toothpaste lava." The surface of this subtype forms a series of plates and is surrounded by other forms of spiny lava (Rowland & Walker, 1987). Although not strictly a flow margin, HAW-13a mostly aligns with the margin of the largest primary lobe mapped by Rowland and Walker (1987) (their Figure 1) and could plausibly be misinterpreted as a flow margin in remotely-sensed data. This margin interval therefore provides a useful reference to evaluate the potential for lava flow characterization in the absence of ground truth.

2.2.3 Blocky ʻaʻā (Highway flow)

Finally, we include a margin interval from a lava that may be intermediate between block lava and ʻaʻā. This interval (IDA-01) comes from the margin of the informally named "Highway" flow (Figure 1h) at Craters of the Moon National Monument and Preserve in Idaho, USA (Hughes et al., 2019; Kuntz et al., 1982; Tolometti et al., 2020).

Classic block lavas have thicknesses of tens or even hundreds of meters and are covered in angular blocks or sub-rounded boulders (Harris et al., 2017). Their surface is generally vesicle-poor but may have highly vesicular bands (Harris et al., 2017). Highway flow is ~15 m

thick. Its surface includes both rough, viscously-torn slabs, analogous to ʻaʻā clinker, and fractured blocks (Hughes et al., 2019; Kuntz et al., 1982; Tolometti et al., 2020). This surface generally has low vesicularity but isolated regions of high vesicularity are exposed on ~1–2% of the surface (Hughes et al., 2019; Sandmeyer et al., 2017).

This flow is among the most evolved of those tested in the area. Chemical analyses typically measure ~62–65 wt% SiO_2 (Kuntz et al., 1985; Leeman et al., 1976; Stout et al., 1994; Tolometti et al., 2020) and qualify the flow as a trachyte or trachydacite (Stout et al., 1994; Tolometti et al., 2020). Although lavas on Mars, for example, generally have more primitive compositions than that of Highway flow, Christensen et al. (2005) measured ~60–63% SiO_2 for one flow using data from the Thermal Emission Imaging System on board Mars Odyssey (Philip R. Christensen et al., 2004). The alpha proton x-ray spectrometer on the Mars Pathfinder rover also measured rocks in situ with similar SiO_2 content (Economou, 2001; Rieder et al., 1997).

As the single non-mafic margin interval in the present study, the results for IDA-01 cannot be confidently interpreted as general. However, these results nonetheless provide a valuable supplement to the results of other workers at different scales (Bruno et al., 1994; Pyle & Elliott, 2006; Wroblewski et al., 2019).

2.3 Topographic context

There is generally a paucity of meter-scale topographic data available for planetary surfaces and remote terrestrial surfaces, and in high-resolution visual images, shadowing suggestive of the topographic context may be absent if relief is subtle or lighting conditions are ill-suited. Therefore, it may not be possible to independently identify the presence of topographic confinement or significant slopes at meter scales for these locations. Even where sufficiently high-resolution topographic data are available (e.g., Kirk et al., 2008; Moratto et al., 2013; Shean et al., 2016), knowledge of the respective effects of slopes and confinement on empirical margin fractality is essential to interpreting flows in those settings.

Bruno et al. (1994) examined three margin intervals on significant slopes. All three intervals came from 1972 Mauna Ulu ʻaʻā flows on respective slopes of 11.6°, 14.7°, and 27.8°. Bruno et al. (1994) reported significant modification of empirical fractality only for the margin on the steepest slope and therefore infer a critical slope angle in the range 15–28°. To further explore the lower end of this range and determine whether any modification of empirical fractality has a scale-dependent component, we include in the present study a 1971 Mauna Ulu ʻaʻā flow on a slope of ~15° (HAW-15).

The potential for topographic confinement to modify margin fractality has long been recognized (Bruno et al., 1992). However, to our knowledge, no fractal analysis of such a topographically-confined margin has yet been reported. We therefore collected a second Holuhraun margin interval (ICE-02; inset of Figure 1f) that was strongly confined by the right bank of a preexisting stream channel (Bonnefoy et al., 2019). Because both Holuhraun intervals are dominated by spiny pāhoehoe (Voigt et al., 2017), comparison of the confined and relatively unconfined intervals facilitates direct evaluation of the effects of topographic confinement.

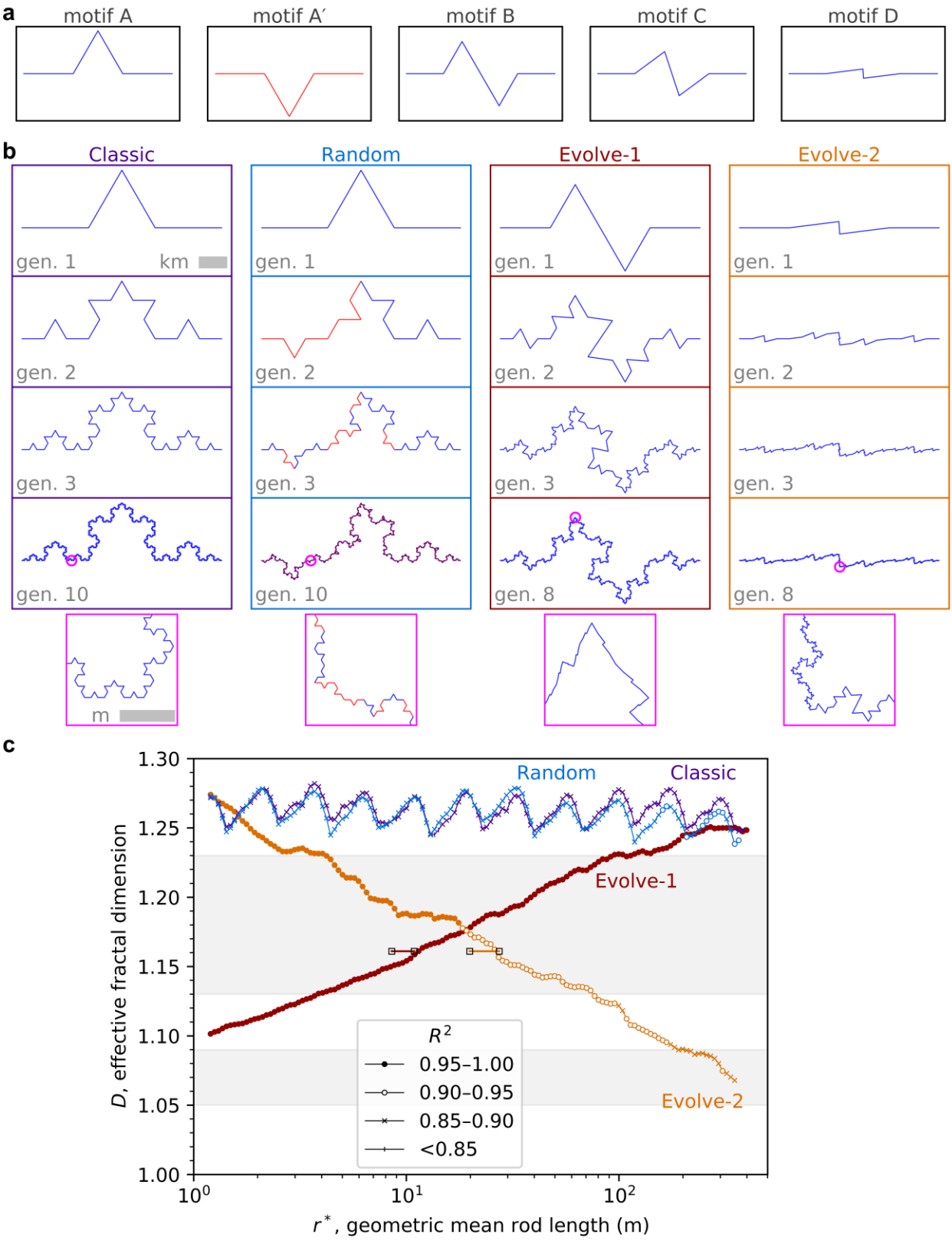

Figure 2. Construction and fractal analysis of some illustrative synthetic geometries. (a) Example motifs used in constructing the geometries. (b) Each geometry is constructed iteratively: generation 1 is a motif from (a), and in each successive generation, every line

segment is replaced by a motif. Classic uses only motif A. For Random, motif A and its flipped counterpart motif A′ each have a 50% chance of replacing any segment. Evolve-1 begins with motif B at generation 1, but the motif used at each later generation evolves, by incrementally shortening the middle segment, passing through motif C and culminating with motif D at generation 8. Evolve-2 has the opposite sequence, beginning with motif D and progressing through motif C to motif B at generation 8. Each final geometry has mean segment lengths of 11.8–12.4 cm. All segment lengths are equal for Classic and Random but vary by a factor of 70 for Evolve-1 and Evolve-2 at generation 8. This variation is evident in the magenta-outlined magnified views, which have equal map scale. (c) The results of scale-dependent fractal analysis, or "fractal scale-spectra", for the final geometries from (b). The theoretical fractal dimension value for both Classic and Random is $D = \frac{\ln(4)}{\ln(3)} \cong 1.26$ (B. Mandelbrot, 1967), which is reasonably approximated by the analysis. (See also Figure S1 of the Supporting Information.) Motif C is applied at generation 4 for Evolve-1 and at generation 5 for Evolve-2, and has a theoretical $D = \frac{\ln(5)}{\ln(4)} \cong 1.16$ (B. Mandelbrot, 1967). For Evolve-1 and Evolve-2, a horizontal line at this D value is drawn between the mean and median segment lengths of the corresponding generation. The intersection of these horizontal lines with the Evolve-1 and Evolve-2 scale-spectra suggests that r^* is a reasonable approximation of the scale to which the measured D is sensitive. The pale gray bands are as in Figures 4–6, for reference, and markers indicate R^2 values (section 3.2.2).

3 Methods

3.1 Field measurement techniques

To collect margin interval vertices in the field, we used differential global navigation satellite system (differential GNSS) receivers to collect margin interval vertices. We used two GNSSs: the Global Positioning System (GPS) and the Global Navigation Satellite System (GLONASS).

We walked the length of each margin interval with a differential GNSS rover while a differential GNSS base station simultaneously collected data. In each case, the rover and base station were both Trimble R8s or both Trimble R10s. Depending on the reliability of line-of-sight communication between the rover and base station, we used a sampling interval that was either spatial (e.g., collect one vertex every 10 cm), which requires continuous line-of-sight communication to support a real-time kinematic correction, or temporal (e.g., collect one vertex each second). Table 1 records the resulting variability in inter-vertex spacing.

We postprocessed each vertex using the Trimble Business Center software. The reported horizontal precision is ≤ 3 cm for all vertices. However, we observed the rover mast to slightly tilt at times. Based on visual assessment, we estimate our measurement error relative to the true margin to average ~15 cm (which corresponds to a tilt of ~4°). To better simulate the plan-view geometry of orthorectified or nadir-pointing images, all analyses use only the x- and y-coordinates of the postprocessed vertices.

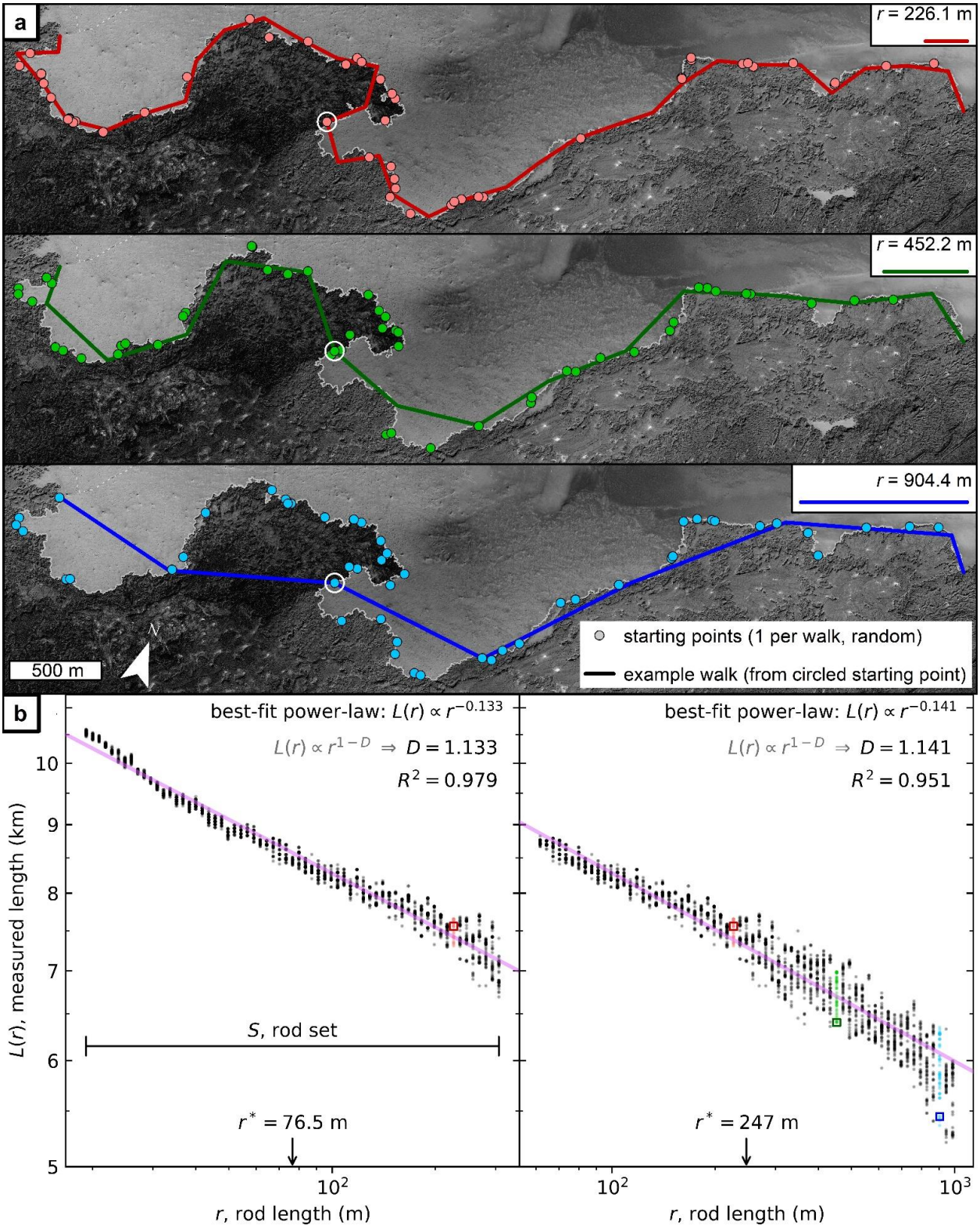

Figure 3. Examples from the fractal analysis of margin interval ICE-01a by the divider method (section 3.2.2). (a) Example data for three different rod lengths. ICE-01a is drawn in light gray. Background is 2015 visible data from Loftmyndir ehf. (0.5 m/pixel). For each rod length, the random starting points for all 50 walked paths are shown as colored dots. Also shown is a single

example path walked with each rod length, starting from the white-circled starting point in each pane. (b) Two log–log Richardson plots. Each shows 50 measured lengths (with each length measured from a different starting point) for each of 65 different rod lengths. The 65 rod lengths in each plot form a rod set. The three selected rod lengths (r values) and their colors correspond between (a) and (b), with the example walks from (a) marked by squares in (b). The representative scale, r^*, is the geometric mean rod length for each rod set (Richardson plot), or equivalently, the median rod length. The effective fractal dimension D is calculated from the trend (which is linear in a log-log plot) of the best-fit power-law (pastel purple), as indicated. The coefficient of determination R^2 measures the goodness of fit and has a maximum of unity (section 3.2.2). The compiled D values from many rod sets analyzing the same margin interval form a fractal scale-spectrum (e.g., Figure 2c). Two Richardson plots are shown to (1) highlight the reuse of results for the same rod length r between different rod sets, such as the results for $r = 226.1$ m (red dots), which appear in both plots, and (2) provide examples of two different R^2 values.

3.2 Fractal analysis

3.2.1 Natural fractality

How the measured fractality of natural geometries should be interpreted has been much debated (e.g., Avnir et al., 1998; Shenker, 1994). Early workers (e.g., B. Mandelbrot, 1967) interpreted such fractality to imply statistical self-similarity. In strictly self-similar geometries, such as the classic Koch curve (Classic in Figure 2), identical geometric patterns are observed when the fractal is viewed across a wide range of scales (B. Mandelbrot, 1967). For a statistically self-similar geometry, on the other hand, comparable but not identical geometric patterns repeat across a wide range of scales. The random Koch curve (Random in Figure 2) is one such example (Falconer, 2003).

More recently, Mandelbrot (2002) urged greater caution in interpreting natural geometries to be self-similar. Additionally, Gneiting and Schlather (2004) presented a family of synthetic geometries that have formally-defined fractality but are not self-similar, and Li and Li (2017) have since used this family to describe natural phenomena, namely, sea level fluctuations. In this work, we interpret measured fractality to describe the tortuosity of a line rather than imply statistical self-similarity. Likewise, we interpret the effective fractal dimension D as a summary statistic that describes tortuosity over a scale range.

3.2.2 Overview of the divider method

Different fractal analysis methods can yield different effective fractal dimension (D) values (e.g., Gneiting et al., 2012; B. Klinkenberg & Goodchild, 1992). Moreover, such discrepancies have been specifically reported for lava flow margins (cf. Bruno et al., 1994; Gaonac'h et al., 1992; Luongo et al., 2000). We choose to use the divider method to support comparison to both the large catalog of Bruno et al. (1994) and to most other studies lava margin fractality (e.g., Blake & Bruno, 2000; Bray et al., 2018; Pyle & Elliott, 2006; Wroblewski et al., 2019).

In the divider method (Figure 3) (Richardson, 1961), a rod of a specified length r_1 is walked along the length of a geometry, such as a lava margin. The apparent length $L(r_1)$ of that

geometry, as measured by the rod, is recorded. This same procedure is then repeated with n different rods, each of a different length r_i. If the apparent lengths $L(r_i)$ versus the respective rod lengths r_i used to make those measurements follow a power-law decay, the effective fractal dimension D can be calculated from the best-fit $L(r) \propto r^{1-D}$. Equivalently, these measurements would follow a linear trend with negative slope m on a log–log plot (Figure 3b)—often called a Richardson plot in this context—and the fractal dimension could be calculated from $D = 1 - m$.

Following previous workers (e.g., Bruno et al., 1994), we interpret a lava flow margin interval to be empirically fractal if the best-fit $L(r) \propto r^{1-D}$ reasonably describes the trend of the data, as quantified by the coefficient of determination R^2. Throughout this work, we use "empirical" or "measured" fractality to signal this interpretation of fractality and distinguish it from analytical definitions (cf. Falconer, 2003; Benoit B. Mandelbrot, 1982). Similarly, and following Mandelbrot (1982), we refer to fractal dimensions determined by measurement rather than from theory as effective fractal dimensions but use the variable D for both theoretical and effective fractal dimensions. To calculate R^2, we use the formula $R^2 = 1 - \sum_{i=1}^{n}(\hat{y}(r_i) - y_i)^2 / \sum_{i=1}^{n}(y_i - \bar{y}_i)^2$, which supports comparison between linear and nonlinear fits and is one of the formulae recommended by Kvålseth (1985). We perform model fitting using the version of the Levenberg–Marquardt algorithm described by Moré (1978), as implemented in SciPy, a scientific computing package in the Python programming language.

3.2.3 Selection and stepping of rods

To avoid overrepresenting the inter-vertex segments or measurement error in our results, we set the shortest rod used for each margin interval equal to the larger of twice the mean inter-vertex spacing (Andrle, 1992) (Table 1) and twice the estimated measurement error of ~15 cm (section 3.1). Each successively longer rod has a length $r_i = f r_{i-1}$, where $f > 1$. Such geometric spacing is generally used in fractal analysis (Brian Klinkenberg, 1994) and reflects the scaling of empirical fractals. Following Bruno et al. (1992, 1994), the largest rod used for each margin interval must walk that interval in no fewer than five steps (including the fractional steps described in the next paragraph).

With each rod (Figure 3a), we start walking at a randomly selected point along the margin interval (which is generally not at a vertex) to avoid overrepresenting any particular subset of coordinates (Andrle, 1992). Once the rod has been walked to the end of the margin interval, we restart walking from the randomly-selected point in the opposite direction and sum the lengths measured in each direction (Andrle, 1992). When the final step of a walk would overshoot the end of a margin interval (as is generally the case), the residual straight-line distance to the end vertex is added to the measured length. This addend is intended to mitigate systematic error (Andrle, 1992; Brian Klinkenberg, 1994). The entire procedure is then repeated 49 more times with each rod, each time from a newly selected random point, following Andrle (1992).

3.2.4 Rod sets and rod set sequences

The scale dependence of the effective fractal dimension D is a major focus of the present study but has not been emphasized in previous studies of lava margins (section 2.1) or other geomorphic features (Andrle, 1996b, 1996a). D must be calculated over a range of scales. Therefore, to describe the scale dependence of D, we must calculate D over many scale ranges for each margin interval. Each such scale range is defined by the range of rod lengths used in the

analysis. We refer to the sequence S of rod lengths r that span such a scale range as the "rod set" for that analysis (Figure 3b). Thus, for each analysis k, which yields a single D value, $S_k = (r_{i=1}, r_{i=2} \ldots r_{i=n})|_k$. For simplicity of reference, and following Andrle (1992), we will treat the geometric mean of a rod set $r^* = (\prod_{i=1}^{n} r_i)^{1/n}$ as the representative scale of that rod set. Because each rod set in the present study is composed of an odd number ($n = 65$) of logarithmically-spaced rod lengths, r^* is also the median rod length of each rod set. Although r^* is a non-rigorous convenience, it provides a plausible reference value (Figure 2c).

To define a rod set, any two of three interdependent parameters must be specified: the inter-rod factor $f = r_{i+1}/r_i$, the number of rods n in the rod set, and the factor-range of the rod set $F = r_n/r_1$. Andrle (1992) observed that a larger n reduced random scatter in the calculated D values but also noted that a larger F would yield a poorer model fit in the presence of any systematic divergence from a power-law trend (e.g., curvature on a Richardson plot; Figure 3b). On that basis, he suggested the use of a large n and a small F. However, we interpret D as a summary statistic that describes tortuosity over a scale range, roughly analogous to a moving average of scale-dependent tortuosity (where the averaging window moves along the r^* axis). In that interpretation, F should be sufficiently large to avoid variability due to random noise but not larger than that, to preserve as much scale resolution as possible and support as many rod sets as possible for a given geometry.

Guided by these goals, we use $F = 16$ and $n = 65$, implying $f = F^{1/(n-1)} = 16^{1/64} \cong 1.044$, throughout the present study. These parameters satisfy the recommendation $n \geq 5$ of Klinkenberg (1994) and facilitate comparison to the field analysis results of Bruno et al. (1994), who preferred $F = 16$ or 32, $n = 5$ or 6, and $f = 2$ for margin intervals as long as those in the present study (section 2.1). Each D value is therefore calculated by fitting 3250 apparent lengths (Figure 3b), which come from 50 iterations with each of 65 rod lengths in a rod set. The D value for each rod set is plotted against r^* on a log–log plot. We call the entire sequence of scale-dependent D values plotted for a given margin interval a "fractal scale-spectrum" (cf. Figure 7 of Andrle (1992) and Figure 4 of Maria and Carey (2002)). For example, the fractal scale-spectra in Figure 2c reflect how the tortuosity of Evolve-1 and Evolve-2 vary with scale.

The ratio between the corresponding scales (e.g., minimum, maximum, representative) of consecutive rod sets is the inter-rod-set factor $I = (r_i|_{k+1})/(r_i|_k)$. We invariably set $I = f$ throughout this study. This correspondence permits rod-stepping results to be reused between overlapping rod sets, because $r_i|_k = r_{i-1}|_{k+1}$ (e.g., red dots in both plots of Figure 3b). This reuse facilitates an extreme savings in computation time. Unfortunately, this reuse also reduces the independence of D values calculated with overlapping rod sets. Nonetheless, the use of 50 iterations (starting points) sufficiently reduces variability in calculated D values (Andrle, 1992) that the reuse of rod-stepping results has no significant effect on our general results.

3.2.5 Comparison to the Hurst exponent

For reference, we note another measure, called the Hurst exponent. The Hurst exponent has been used to characterize rough geologic surfaces in both terrestrial and planetary contexts (Neish et al., 2017; Shepard et al., 1995, 2001). Though fractality is often discussed when applying the Hurst exponent, the measure is generally independent of fractality (Gneiting & Schlather, 2004). Nonetheless, in the special case of self-similar geometries (section 3.2.1), the

Hurst exponent H is simply related to D by $D = H - 3$ for surfaces and $D = H - 2$ for profiles (e.g., Shepard et al., 1995).

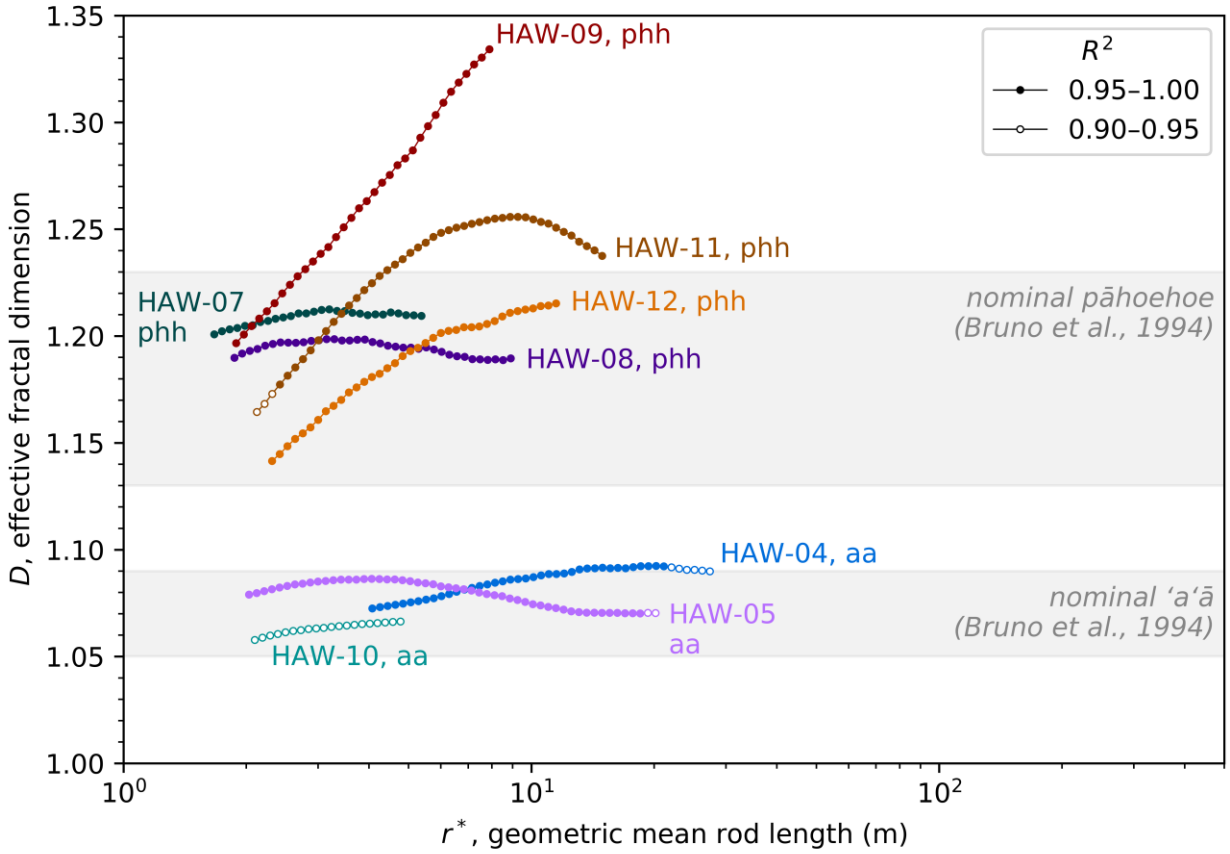

Figure 4. Fractal scale-spectra for ʻaʻā (HAW-04, -05, and -10) and pāhoehoe (HAW-07, -08, -09, -11, and 12) margin intervals. Warm-colored spectra in Figures 4–6 have D ranges >0.05 after excluding results for which $R^2 < 0.95$, suggesting scale dependence (section 4.1). None of these margin intervals have acute topographic effects. See Table 1 for explanation of morphologic codes (e.g., phh).

4 Results

The fractal analysis results for ʻaʻā and pāhoehoe margin intervals on shallow slopes (generally $\lesssim 4°$), that lack substantial topographic confinement, are presented in Figure 4. The results for other morphologic types that likewise are not subject to acute topographic effects are presented in Figure 5. Finally, the results for an ʻaʻā margin interval on a 15° slope (HAW-15) and a spiny pāhoehoe margin interval confined by a stream channel (ICE-02) are presented in Figure 6. In these plots, scale-invariant behavior is indicated by a constant fractal dimension D as the geometric mean rod length r^* changes, and hence, a horizontal trend. Conversely, scale-dependent behavior is indicated by variation in D as r^* changes.

4.1 Scale dependence

In general, the examined margin intervals exhibit a wide range of scale-dependent to relatively scale-independent empirical fractal behavior. For discussion purposes, we will adopt the criteria of Bruno et al. (1994) in this section to identify scale-dependent empirical fractality. However, other reasonable criteria would not fundamentally alter this discussion. Bruno et al. (1994) discarded all fractal analyses for which $R^2 \leq 0.95$ or for which slope or topographic confinement are significant. Twelve margin intervals satisfy these criteria. Bruno et al. (1994) further interpreted empirical fractality to be scale-independent if the observed variation in D was $\lesssim 0.05$. Based on that criterion, 7 of the remaining 12 margin intervals (HAW-04, HAW-05, HAW-07, HAW-08, HAW-13a, IDA-01, and IDA-03) have scale-independent empirical fractality, with observed D variation of 0.01–0.05, and 5 (HAW-09, HAW-11, HAW-12, ICE-01a, and IDA-02) have scale-dependent empirical fractality, with observed D variation of 0.07–0.17. For reference, note that relaxing the minimum required R^2 to 0.90 (Anderson et al., 2005; You et al., 1996) would cause 13 margin intervals to be included: HAW-10 would be added to the list of scale-independent margin intervals (Figure 4) and IDA-03 and HAW-13a would switch from scale-independent to scale-dependent, with D variations of 0.08 and 0.06, respectively (Figure 5).

Returning to the $R^2 > 0.95$ criterion, all five of the margin intervals with scale-dependent empirical fractality have a maximum effective fractal dimension $D_{\max} \gtrsim 1.19$. The fact that margin intervals with lower $D_{\max}$ values do not exhibit greater variation in D may partially reflect their proximity to the lowest possible value $D = 1$. However, one cannot generalize that margin intervals with low D values have little variation in D and margin intervals with high D values have large variation in D. For example, D values measured for IDA-02 range from the relatively low $D_{\min} \sim 1.08$ at $r^* \sim 1.20$ m to the relatively high $D_{\max} \sim 1.25$ at $r^* \sim 35.2$ m, a span of ~ 0.17. For comparison, 24 of the 27 margin intervals measured by Bruno et al. (1994) in the field fall in the same range of D values, 1.08–1.25, measured for IDA-02 alone, including all pāhoehoe and transitional margin intervals and most (4 of 7) ‘a‘ā margin intervals. At the other extreme of variability, two pāhoehoe intervals from the same margin on Mauna Ulu, HAW-07 and HAW-08, each have D values that vary by ~ 0.01 across the analyzed scales (r^* of 1.67–5.37 m and r^* of 1.87–8.90 m, respectively), despite having $D_{\min} \gtrsim 1.20$.

4.2 Topographic effects

Two margin intervals are subject to acute topographic effects and therefore violate what Bruno et al. (1994) called their “simple-case” criteria (Figure 6). To enable some useful comparisons, we will only exclude in the present section those results for which $R^2 \leq 0.90$, similar to You et al. (1996) and Anderson et al. (2005). Nonetheless, the general behavior described here is at least suggested by those results that meet the more restrictive $R^2 > 0.95$ criterion (cf. section 4.1).

Compared to the other three ‘a‘ā margin intervals, HAW-15, on a slope of 15°, has much lower D values. Its $D_{\max}$ is 1.05, measured at $r^* = 1.20$ m. No other margin interval in this study, except for the topographically-confined ICE-02, has a D value as low at any analyzed scale, and the lowest D value measured by Bruno et al. (1994) on a slope ≤15° was likewise 1.05. HAW-15’s $D_{\min}$ is 1.02, measured at $r^* = 16.9$ m, which is the lowest D measured in the

present study. The lowest D reported by Bruno et al. (1994) was also 1.02 and was measured for another Mauna Ulu ʻaʻā margin interval on a 28° slope.

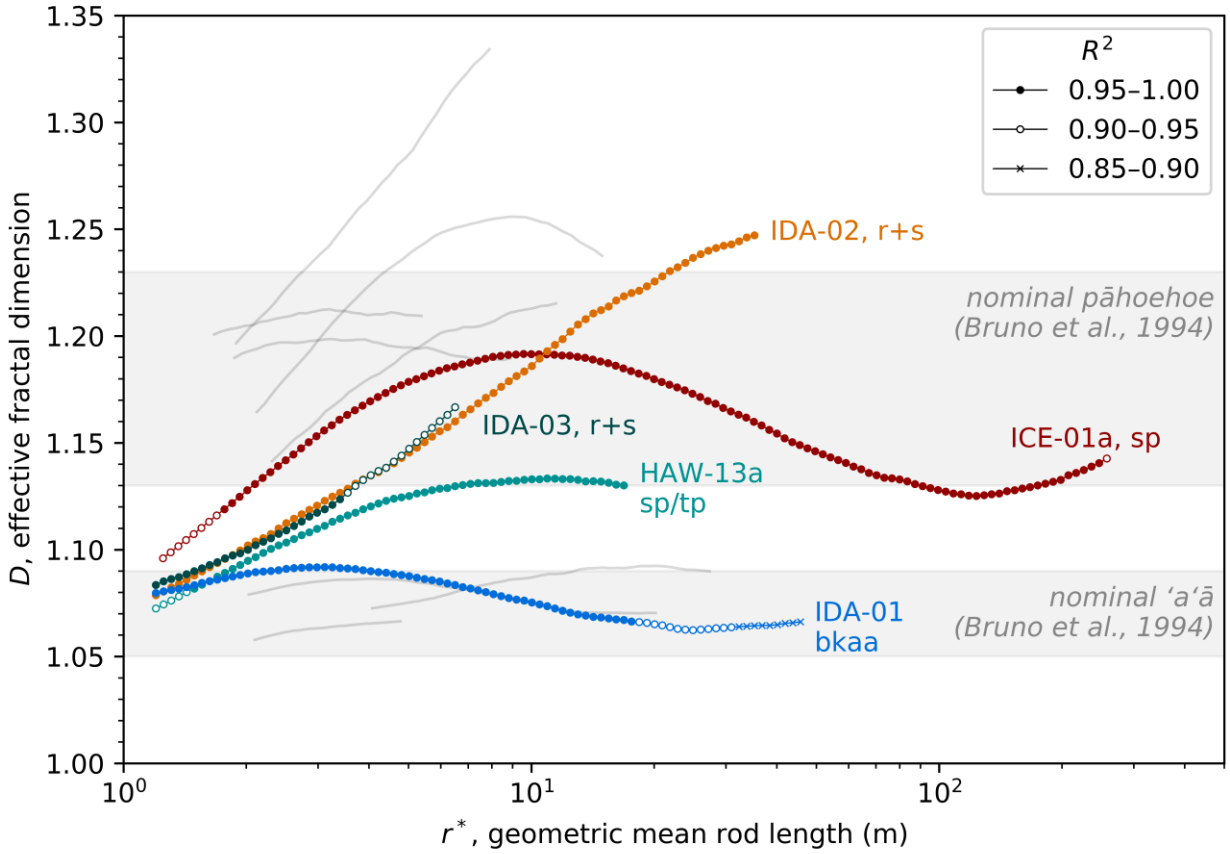

Figure 5. Fractal scale-spectra for spiny pāhoehoe (ICE-01a), blocky ʻaʻā (IDA-01), rubbly and slabby lava (IDA-02 and IDA-03), and primary toothpaste (HAW-13a) margin intervals, with fractal scale-spectra from Figure 4 shown as unmarked gray lines, for comparison. None of these margin intervals have acute topographic effects. Warm colors have the same meaning as in Figure 4. See Table 1 for explanation of morphologic codes (e.g., r+s).

D values for the Holuhraun margin interval confined by a stream channel, ICE-02, are likewise much lower than D values measured at the same scales for the relatively unconfined Holuhraun margin interval, ICE-01a. Over r^* of 1.25–19.1 m, and requiring $R^2 > 0.90$, D values measured at equivalent scales are 0.037–0.146 less for ICE-02 than for ICE-01a. The respective ranges of D values over those scales are also disjoint: D of 1.04–1.07 for ICE-02 but D of 1.10–1.19 for ICE-01a.

5 Discussion

5.1 Consequences for interpretation

5.1.1 Intrinsic variability of basaltic lava margins

Our analyses of ‘a‘ā and pāhoehoe margin intervals (Figure 4) reproduce the general results of comparable analyses by Bruno et al. (1994). Namely, these results are that ‘a‘ā and pāhoehoe margins have distinct typical D ranges that do not overlap, with the D values of pāhoehoe margins systematically higher than those of ‘a‘ā margins. Our results also largely reproduce the quantitative details of those of Bruno et al (1994). Their field analyses correspond to r^* of 0.5–4 m, with a preference for $r^* = 4$ m and $r^* = 2.83$ m (section 2.1). At $r^* < 4$ m, the results for our three ‘a‘ā intervals (after rounding to the nearest hundredth) all fall within the nominal ‘a‘ā range of 1.05–1.09 that Bruno et al. (1994) identify, though they would have rejected the results for HAW-10 for having $R^2 \leq 0.95$. Similarly, at these scales, only the results for HAW-09 of the five pāhoehoe intervals is outside the nominal pāhoehoe range of 1.13–1.23, at $r^* > 2.7$ m.

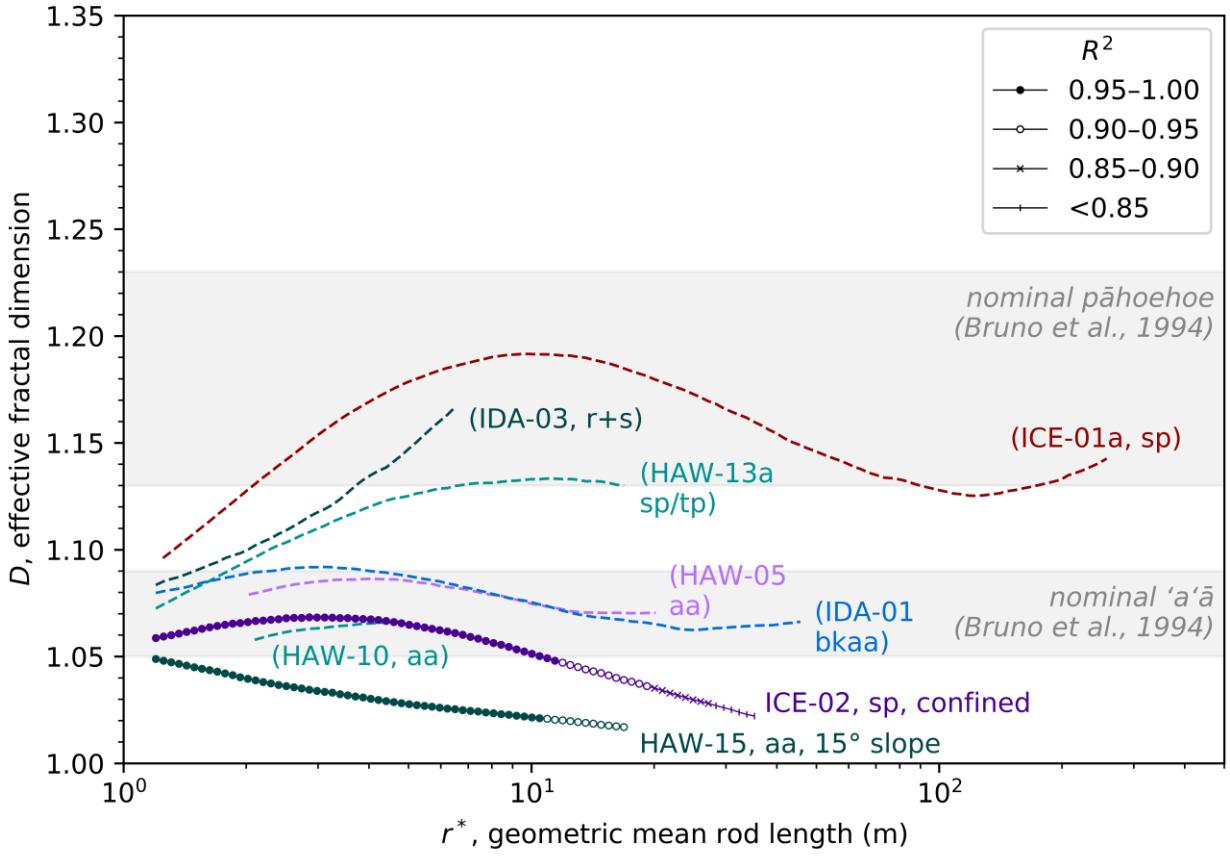

Figure 6. Fractal scale-spectra for ‘a‘ā margin interval on 15° slope (HAW-15) and spiny pāhoehoe margin interval that was confined by a preexisting stream channel (ICE-02). Additional fractal scale-spectra from Figures 4 and 5 for select margin intervals are shown as dashed lines with parenthetical labels and no markers, for comparison: spiny pāhoehoe ICE-01a,

rubbly and slabby lava IDA-03, primary toothpaste HAW-13a, ʻaʻā HAW-05, ʻaʻā HAW-10, and blocky ʻaʻā IDA-01. These additional margin intervals are on shallow slopes ($\lesssim 4°$) and relatively unconfined. Warm colors have the same meaning as in Figure 4. See Table 1 for explanation of morphologic codes (e.g., r+s).

However, our results for other morphologic types significantly complicate this picture (Figure 5). Even if we consider only basaltic margins and exclude results for which $R^2 \leq 0.95$, every analyzed margin interval for a morphologic type other than ʻaʻā and pāhoehoe has at least some D values in the nominal ʻaʻā and/or pāhoehoe ranges of Bruno et al. (1994). Measured D values fall in the nominal pāhoehoe range for spiny pāhoehoe ICE-01a at r^* of 2.01–247 m (rounding D to the nearest hundredth), for rubbly and slabby lava IDA-02 at 3.07–21.9 m, and for primary toothpaste HAW-13a at 6.79–16.9 m. Similarly, D values fall in the nominal ʻaʻā range for rubbly and slabby lava IDA-02 at r^* of 1.20–1.56 m, rubbly and slabby lava IDA-03 at 1.20–1.49 m, and primary toothpaste HAW-13a at 1.49–1.78 m.

Taken together, the widely varying scale dependence of empirical margin fractality among the analyzed intervals and the frequently overlapping D ranges of the analyzed morphologic types indicate that D, when measured with a single rod set, is not a reliable, independent indicator of morphologic type at meter scales (that is, for r^* of 1–10 m). It further seems unlikely that the shape of the fractal scale-spectrum has the potential to serve as a discriminator of morphologic type at meter scales. For example, among pāhoehoe margin intervals, the fractal scale-spectra (Figure 4) for HAW-07 and HAW-08 (Figure 1c) are distinctly different from those of HAW-09 (Figure 1d), HAW-11, and HAW-12.

Moreover, primary toothpaste HAW-13a, which is the only interval along an internal subtype margin (section 2.2.2), does not have a distinguishing scale-spectrum. Although primary toothpaste is a subtype of spiny pāhoehoe, its scale-spectrum nearly coincides with that of rubbly and slabby lava IDA-03 over r^* of 1.49–3.39 m (excluding results with $R^2 \leq 0.95$) (Figure 5). The curvature of the HAW-13a scale-spectrum is also similar to that of the spiny pāhoehoe ICE-01a scale-spectrum, and the results for HAW-13a have high R^2 values (>0.90 and typically >0.95) similar to those for flow margin intervals. These observations suggest that subtype margins within flows may not be readily distinguished from flow margins by their fractality (cf. Anderson et al., 2005).

5.1.2 Margins of non-mafic composition

For blocky ʻaʻā IDA-01, which has intermediate composition, we measure D values of 1.07–1.09 for r^* of 1.2–17.6 m (which use r of 0.3–70.4 m). This result is in reasonable agreement with those of Bruno et al. (1994), who measured D values of 1.08–1.17 for $r < 31.6$ m and 1.09–1.20 for r of 31.6–100 m among five margin intervals of basaltic andesite. (Bruno et al. (1994) do not specify the rods used and therefore r^* cannot be calculated.) At coarser scales, Bruno et al. (1994) measured systematically higher D values. For example, they reported D values of 1.20–1.46 for four of these margin intervals at r of 316–1995 m. They therefore concluded that margin intervals of intermediate composition, unlike those of mafic composition (cf. section 4.1), have scale-dependent fractality. Moreover, they speculated that lower D values at fine scales may be due to the suppression of nonlinear flow dynamics at these scales, resulting in non-fractality.

However, we note that the fractal scale-spectra for IDA-01, which has intermediate composition, and HAW-05, which has basaltic composition, nearly coincide across their overlapping scales, r^* of 2.03–20.3 m (requiring $R^2 > 0.90$) (Figure 6). This correspondence suggests that margin intervals of intermediate composition are not necessarily less fractal than those of basaltic composition and that fractal analysis may not be able to distinguish between ʻaʻā margin intervals, like HAW-05, and blocky ʻaʻā margin intervals, like IDA-01. Similarly, Pyle and Elliott (2006) concluded that fractal analysis with a single rod set cannot discriminate between basaltic ʻaʻā margins and dacitic blocky ʻaʻā margins based on analysis of 10 dacitic blocky ʻaʻā margin intervals from the Kameni Islands, Greece at $r^* = 10$ m (r of 1–100 m). In addition, Wroblewski et al. (2019) calculated single-r^* D values of 1.03–1.11 at r^* of 152–802 m for five subaerial margin intervals of intermediate to felsic composition. It is not currently clear how these relatively low D values relate to the higher D values measured by Bruno et al. (1994) at similar (coarse) scales and for similar compositions.

5.1.3 Topographic context

Interpretation of morphologic type from margin fractal analysis is further complicated by topographic context (Figure 6). The margin interval from a Mauna Ulu ʻaʻā flow on a 15° slope, HAW-15, generally has very low D values. These D values are lower than those of any other margin interval in the present study and lower than any result of Bruno et al. (1994) for a margin interval on a shallower slope. These observations strongly suggest that HAW-15's D values are depressed relative to the intrinsic D of an ʻaʻā margin interval. That is, these are lower than the D values that would be expected for a similar flow margin interval on a shallow slope without topographic confinement.

Similarly, Bruno et al. (1994) measured their lowest D value, 1.02, for another Mauna Ulu ʻaʻā margin interval on a 28° slope. Based on that observation, they likewise inferred that steep slopes could depress D values. However, they also calculated an unusually low $R^2 = 0.78$ for that interval. This result led them to conclude that empirical "fractal behavior… break[s] down, with an accompanying decrease in D, on steep (>15–28°) slopes." Conversely, the results for HAW-15 have $R^2 > 0.95$ across most analyzed scales (namely, for r^* of 1.20–10.5 m). These high R^2 values indicate that a margin's D can be significantly depressed by steep slopes without an associated loss of empirical fractality. Interestingly, Bruno et al. (1994) measured their two lowest D values at field scales for two Mauna Ulu ʻaʻā margin intervals on slopes of 11.6° and 14.7°, with $R^2 = 0.99$ for both results. These observations could likewise suggest depressed D values combined with retention of empirical fractality, though the intrinsically low D values of ʻaʻā margins complicates that interpretation.

Comparison of the results for spiny pāhoehoe ICE-02, which is confined by a channel, to those of its relatively unconfined counterpart, ICE-01a, strongly suggests that the D values of ICE-02 are also depressed. In addition, the results for ICE-02, like those for HAW-15, have $R^2 > 0.95$ across meter scales (namely, for r^* of 1.20–11.4 m). However, the topographic relief is distinctly different in each case. For HAW-15, flow is down dip and the 448 m margin interval falls 88 m vertically along its length. For ICE-02, flow is along strike and parallel to a bank ~10 m high (Bonnefoy et al., 2019, including their Figure 10). Moreover, when we observed the margin in August 2015, the surface relief along portions of the interval was as low as ~2 m due to post-eruption fluvial modification (Bonnefoy et al., 2019, including their Figure 12).

The results for both HAW-15 and ICE-02 indicate that margin D values can be significantly depressed at meter scales by local topography without destroying empirical fractality. Therefore, low R^2 values for margin fractal analyses cannot be relied upon to recognize and exclude results modified by topography. In the absence of independent knowledge of local topography, a margin with low measured D may indicate a morphologic type with intrinsically low D, such as ʻaʻā, or a morphologic type with intrinsically high D, such as pāhoehoe, that was topographically confined or emplaced on a slope. Moreover, even where topographic data are available, one must consider the potential that terrain adjacent to a lava margin was modified post-emplacement, as occurred along the ICE-02 interval. In the case of such modification, the extant surface relief could be below the vertical resolution of the data even if the original constraining height had been much greater.

5.1.4 Constraints provided by margin fractal analysis

The fractal analysis of lava margins retains some interpretive power despite the complexities that we have discussed (sections 5.1.1–5.1.3). The results reported by Bruno et al. (1994) and by us in the present study strongly suggest that the intrinsic D values of pāhoehoe margins are consistently high, say, ≥1.13 (cf. Bruno et al., 1994), regardless of scale. This behavior supports a reasonable statistical exclusion test, subject to some caveats: pāhoehoe would be unlikely to dominate the margins of lava flows in a flow field or region if measured D values for many margin intervals in that location are consistently <1.13. The value of this test is notably enhanced if pāhoehoe is the typical morphologic type of large lava deposits, as hypothesized by Self et al. (1998).

Two important caveats to this test are that acute topographic effects must be rare or absent among the targeted flows (see section 5.1.3) and the margins must be geomorphically fresh. To date, all major studies that have aimed to develop the interpretive potential of margin fractal analysis (Anderson et al., 2005; Blake & Bruno, 2000; Bruno et al., 1992, 1994; Gaonac'h et al., 1992; Wroblewski et al., 2019) have exclusively targeted geomorphically fresh flows, like the present study. However, erosion, mass wasting, and sediment mantling are likely to modify margin D values (Campbell & Campbell, 1992; Chase, 1992; Lifton & Chase, 1992; Schaefer et al., 2020). Aeolian and fluvial erosion roughen topography, and we would therefore expect such erosion to render margins more tortuous and increase their D values (Chase, 1992; Lifton & Chase, 1992). Conversely, mass wasting is a diffusive process and smooths topography, so we would expect it to smooth margins and lower their D values (Chase, 1992; Lifton & Chase, 1992). Sediment mantling also generally smooths topography (Chase, 1992; Lifton & Chase, 1992). However, rather than modifying a lava flow in situ, like erosion and mass wasting, mantling shifts the lava–sediment margin inward such that it becomes analogous to a topographic contour of the flow's rough surface (Schaefer et al., 2020). In preliminary results from Holuhraun, we (Schaefer et al., 2020) found that this mantling therefore increased D, but this result may not be general. Another important caveat to the proposed test is that the flow must have been emplaced subaerially, as the margin fractality of submarine flows has not been extensively explored and existing results are ambiguous (Maeno et al., 2016; Mitchell et al., 2008; Wroblewski et al., 2019).

5.2 Our results in context

5.2.1 Scale dependence

Our study focuses primarily on meter scales, or more precisely, r^* of ~1–10 m. Across these scales, we observe significant variation in measured D values for 5 of the 12 margin intervals that meet the criteria of Bruno et al. (1994) (section 4.1). (Of the 15 margin intervals that we analyzed, Bruno et al. (1994) would have excluded HAW-15 and ICE-02, which are acutely affected by topography, and HAW-10, for which no measurement attained $R^2 > 0.95$.) At first glance, these results would appear to conflict with those of Bruno et al. (1994). Bruno et al. (1994) report no systematic differences in D between their 27 field analyses, which used r of 0.125–16 m and preferred $r^* = 4$ m and $r^* = 2.83$ m, and their 17 photographic analyses, which used r of 12–2400 m. For three margins, but different intervals, they also directly compared the D values measured in the field to those measured from photographs at coarser scales and found differences similar to along-length variations in D measured at a single r^*.

We propose that our results and those of Bruno et al. (1994) can be reconciled by considering measurement scale and methodology. Only the field analyses of Bruno et al. (1994) correspond to the meter-scale focus of our study. In those field analyses, Bruno et al. (1994) measured each margin interval with only a single rod set, and therefore, at a single r^*. These measurements are thus equivalent to sampling a single point from each fractal scale-spectrum (e.g., Figure 4). If these fractal scale-spectra vary as widely as those that we report, the scatter of the sampled D values would appear random. Consequently, the variability in measured D that Bruno et al. (1994) report between margin intervals may include scale-dependent variability as well.

5.2.2 Physical interpretation

The interpretation of Bruno et al. (1992, 1994) and Gaonac'h et al. (1992) that basaltic flow margins have scale-independent empirical fractality across decimeter to kilometer scales (see section 5.2.1) led both them and others (Anderson et al., 2005; Blake & Bruno, 2000; C. R. J. Kilburn, 1996) to either speculate on the physical implications of the inferred statistical self-similarity or search for specific physical origins. However, even scale-independent empirical fractality does not imply statistical self-similarity (section 3.2.1). Moreover, we measure scale-dependent fractality for 5 of 12 suitable margin intervals at meter scales (section 4.1), and for ICE-01a and IDA-02 at decameter scales. This scale dependence, as well as the broad range of scale-dependent to relatively scale-independent behaviors that we observe, suggests that physical insights based on the putative self-similarity of lava margins should be viewed with caution. More generally, although fractal analysis facilitates quantitative descriptions of natural geometries, it should not be interpreted necessarily to provide insight into the underlying physics unless such an inference is independently supported by theory (e.g., Avnir et al., 1998; Neuman et al., 2013).

6 Conclusions

In the field, we measured the geometry of 15 geomorphically fresh lava flow margin intervals with decimeter precision. These intervals come from Hawai'i, Iceland, and Idaho and represent a wide variety of morphologic types. Based on multi-scale fractal analysis of these geometries, we make the following conclusions.

1. Across representative scales of 1–10 m, lava flow margins exhibit diverse geometric behaviors. As a result, their empirical fractality varies widely from strongly scale-dependent to relatively scale-independent. This diversity is observed even among flows of the same morphologic type.
2. The respective fractal behaviors of pāhoehoe margins and margins of transitional lava types broadly overlap at meter scales, including both effective fractal dimensions and relative scale dependence. Therefore, these types cannot be confidently distinguished on the basis of margin fractal analysis alone at these scales.
3. Steep slopes and topographic confinement can strongly depress the effective fractal dimension of lava margins. Consequently, margins of morphologic types that have intrinsically low effective fractal dimensions cannot be distinguished from margins of other morphologic types at meter scales unless the detailed topographic context at the time of the flow's emplacement is independently constrained.
4. Nonetheless, if measured D values for many geomorphically fresh margin intervals in a flow field or region are consistently <1.13, pāhoehoe is unlikely to dominate that location if the flows were emplaced subaerially and widespread topographic confinement and steep slopes can be excluded.

Acknowledgments and Data

Work in Hawai'i Volcanoes National Park and Craters of the Moon National Monument and Preserve was conducted under science permits HAVO-2012-SCI-0025, HAVO-2016-SCI-0047, and CRMO-2014-SCI-0004. This material is based in part on work supported by the National Science Foundation Graduate Research Fellowship under Grant No. 2012116373, the University of Western Ontario, the Natural Sciences and Engineering Research Council, the Canadian Space Agency, NASA's Solar System Exploration Research Virtual Institute (SSERVI)/Field Investigations to Enable Solar System Science and Exploration (FINESSE), a Geological Society of America Research Grant, and Dan Cavanagh. Alfred McEwen provided valuable support. Michael Sori, Ali Bramson, Sky Beard, and Sean Peters provided field assistance and constructive discussions that improved this manuscript. Trevor Miller, Stephen Scheidt, Youngmin JeongAhn, Xianyu Tan, and Hester Mallonee also assisted in the field. The Python code used to perform fractal analysis is archived in this in-text reference: (Schaefer, 2020). The geometetries of the 15 margin intervals and the synthetic fractals from Figure 2 have been submitted to PANGAEA (http://www.pangae.de) and are also archived with the code at the aforementioned reference.

References

Anderson, S. W., McColley, S. M., Fink, J. H., & Hudson, R. K. (2005). The development of fluid instabilities and preferred pathways in lava flow interiors: Insights from analog experiments and fractal analysis. *Geological Society of America Special Paper 396*, *2396*(10), 147–161. https://doi.org/10.1130/0-8137-2396-5.147

Andrle, R. (1992). Estimating fractal dimension with the divider method in geomorphology. *Geomorphology*, *5*(1–2), 131–141. https://doi.org/10.1016/0169-555X(92)90061-R

Andrle, R. (1996a). Complexity and Scale in Geomorphology: Statistical Self-Similarity vs. Characteristic Scales. *Mathematical Geology*, *28*(3), 275–293. https://doi.org/10.1007/BF02083201

Andrle, R. (1996b). The west coast of Britain: Statistical self-similarity vs. characteristic scales in the landscape. *Earth Surface Processes and Landforms*, *21*(10), 955–962. https://doi.org/10.1002/(SICI)1096-9837(199610)21:10<955::AID-ESP639>3.0.CO;2-Y

Avnir, D., Biham, O., Lidar, D., & Malcai, O. (1998). Is the Geometry of Nature Fractal? *Science (New York, N.Y.)*, *279*(5347), 39–40.

Blake, S., & Bruno, B. . (2000). Modelling the emplacement of compound lava flows. *Earth and Planetary Science Letters*, *184*(1), 181–197. https://doi.org/10.1016/S0012-821X(00)00278-8

Bonnefoy, L. E., Hamilton, C. W., Scheidt, S. P., Duhamel, S., Höskuldsson, Jónsdottir, I., et al. (2019). Landscape evolution associated with the 2014–2015 Holuhraun eruption in Iceland. *Journal of Volcanology and Geothermal Research*, *387*, 106652. https://doi.org/10.1016/j.jvolgeores.2019.07.019

Bray, V. J., Atwood-Stone, C., Neish, C. D., Artemieva, N. A., McEwen, A. S., & McElwaine, J. N. (2018). Lobate impact melt flows within the extended ejecta blanket of Pierazzo crater. *Icarus*, *301*, 26–36. https://doi.org/10.1016/J.ICARUS.2017.10.002

Bruno, B. C., & Taylor, G. J. (1995). Morphologic identification of Venusian lavas. *Geophysical Research Letters*, *22*(14), 1897–1900. https://doi.org/10.1029/95GL01318

Bruno, B. C., Taylor, G. J., Rowland, S. K., Lucey, P. G., & Self, S. (1992). Lava Flows are Fractals. *Geophysical Research Letters*, *19*(3), 305–308. https://doi.org/10.1029/91gl03039

Bruno, B. C., Taylor, G. J., Rowland, S. K., & Baloga, S. M. (1994). Quantifying the effect of rheology on lava-flow margins using fractal geometry. *Bulletin of Volcanology*, *56*(3), 193–206. https://doi.org/10.1007/BF00279604

Campbell, B. A., & Campbell, D. B. (1992). Analysis of volcanic surface-morphology on Venus from comparison of Arecibo, Magellan, and terrestrial airborne radar data. *Journal of Geophysical Research-Planets*, *97*(E10), 16293–16314. https://doi.org/10.1029/92JE01558

Cashman, K. V., Thornber, C., & Kauahikaua, J. P. (1999). Cooling and crystallization of lava in open channels, and the transition of Pāhoehoe Lava to ’A’ā. *Bulletin of Volcanology*, *61*(5), 306–323. https://doi.org/10.1007/s004450050299

Chase, C. G. (1992). Fluvial landsculpting and the fractal dimension of topography. *Geomorphology*, *5*(1–2), 39–57. https://doi.org/10.1016/0169-555X(92)90057-U

Chowdhury, A. R., Saxena, M., Kumar, A., Joshi, S. R., Amitabh, Dagar, A., et al. (2020). Orbiter high resolution camera onboard chandrayaan-2 orbiter. *Current Science*, *118*(4), 560–565. https://doi.org/10.18520/cs/v118/i4/560-565

Christensen, P R, McSween, H. Y., Bandfield, J. L., Ruff, S. W., Rogers, A. D., Hamilton, V. E., et al. (2005). Evidence for magmatic evolution and diversity on Mars from infrared observations. *Nature*, *436*(7050), 504–509. https://doi.org/10.1038/nature03639

Christensen, Philip R., Jakosky, B. M., Kieffer, H. H., Malin, M. C., McSween, H. Y., Nealson, K., et al. (2004). The Thermal Emission Imaging System (THEMIS) for the Mars 2001 Odyssey mission. *Space Science Reviews*. Springer. https://doi.org/10.1023/b:spac.0000021008.16305.94

Economou, T. (2001). Chemical analyses of martian soil and rocks obtained by the Pathfinder Alpha Proton X-ray spectrometer. In *Radiation Physics and Chemistry* (Vol. 61, pp. 191–197). Pergamon. https://doi.org/10.1016/S0969-806X(01)00240-7

Falconer, K. (2003). *Fractal Geometry: Mathematical Foundations and Applications, Second Edition*. *Wiley & Sons*. https://doi.org/10.1002/0470013850

Finch, R. H. (1933). Block Lava. *The Journal of Geology*, *41*(7), 769–770. https://doi.org/10.1086/624096

Gaonac'h, H., Lovejoy, S., & Stix, J. (1992). Scale invariance of basaltic lava flows and their fractal dimensions. *Geophysical Research Letters*, *19*(8), 785–788. https://doi.org/10.1029/92GL00545

Gneiting, T., & Schlather, M. (2004). Stochastic models that separate fractal dimension and the hurst effect. *SIAM Review*, *46*(2), 269–282. https://doi.org/10.1137/S0036144501394387

Gneiting, T., Ševčíková, H., & Percival, D. B. (2012). Estimators of fractal dimension: Assessing the roughness of time series and spatial data. *Statistical Science*, *27*(2), 247–277. https://doi.org/10.1214/11-STS370

Gregg, T. K. P. (2017). Patterns and processes: Subaerial lava flow morphologies: A review. *Journal of Volcanology and Geothermal Research*, *342*, 3–12. https://doi.org/10.1016/J.JVOLGEORES.2017.04.022

Hamilton, C. W. (2019). "Fill and spill" lava flow emplacement: Implications for understanding planetary flood basalt eruptions. In N. F. Six & G. Karr (Eds.), *Marshall Space Flight Center Faculty Fellowship Program* (p. 9). NASA (TM—2019–220139). Retrieved from https://ntrs.nasa.gov/archive/nasa/casi.ntrs.nasa.gov/20200000048.pdf

Harris, A. J. L., Rowland, S. K., Villeneuve, N., & Thordarson, T. (2017). Pāhoehoe, 'a'ā, and block lava: an illustrated history of the nomenclature. *Bulletin of Volcanology*, *79*(1), 7. https://doi.org/10.1007/s00445-016-1075-7

Holcomb, R. T. (1987). Eruptive history and long-term behavior of Kilauea Volcano. In R. W.

Decker, T. L. Wright, & P. H. Stauffer (Eds.), *Volcanism in Hawaii: U.S. Geological Survey Professional Paper 1350, Volume 1* (pp. 261–350).

Hon, K., Gansecki, C., & Kauahikaua, J. (2003). The Transition from ʻAʻā to Pāhoehoe Crust on Flows Emplaced During the Puʻu ʻŌʻō-Kūpaianaha Eruption. *USGS Prof. Paper 1676*, 89–103. https://doi.org/10.1016/0003-6870(73)90259-7

Hughes, S. S., Haberle, C. W., Kobs Nawotniak, S. E., Sehlke, A., Garry, W. B., Elphic, R. C., et al. (2019). Basaltic Terrains in Idaho and Hawai'i as Planetary Analogs for Mars Geology and Astrobiology. *Astrobiology*, *19*(3), 260–283. https://doi.org/10.1089/ast.2018.1847

Keszthelyi, L., McEwen, A. S., & Thordarson, T. (2000). Terrestrial analogs and thermal models for Martian flood lavas. *Journal of Geophysical Research: Planets*, *105*(E6), 15027–15049. https://doi.org/10.1029/1999JE001191

Keszthelyi, L. (2002). Classification of the mafic lava flows from ODP Leg 183. *Proceedings of the Ocean Drilling Program, Scientific Results*, *183*(February), 1–28.

Keszthelyi, Laszlo, Thordarson, T., McEwen, A., Haack, H., Guilbaud, M. N., Self, S., & Rossi, M. J. (2004). Icelandic analogs to Martian flood lavas. *Geochemistry, Geophysics, Geosystems*, *5*(11), Q11014. https://doi.org/10.1029/2004GC000758

Kilburn, C. R. J. (1996). Patterns and predictability in the emplacement of subaerial lava flows and flow fields. In *Monitoring and Mitigation of Volcano Hazards* (pp. 491–537). Berlin Heidelberg: Springer-Verlag. https://doi.org/doi:10.1007%2F978-3-642-80087-0_15

Kilburn, Christopher R J. (1990). Surfaces of Aa Flow-Fields on Mount Etna, Sicily: Morphology, Rheology, Crystallization and Scaling Phenomena. In J. H. Fink (Ed.), *Lava Flows and Domes: Emplacement Mechanisms and Hazard Implications* (pp. 129–156). Berlin Heidelberg: Springer-Verlag. https://doi.org/10.1007/978-3-642-74379-5_6

Kirk, R. L., Howington-Kraus, E., Rosiek, M. R., Anderson, J. A., Archinal, B. A., Becker, K. J., et al. (2008). Ultrahigh resolution topographic mapping of Mars with MRO HiRISE stereo images: Meter-scale slopes of candidate Phoenix landing sites. *Journal of Geophysical Research*, *113*, E00A24. https://doi.org/10.1029/2007JE003000

Klinkenberg, B., & Goodchild, M. F. (1992). The fractal properties of topography: A comparison of methods. *Earth Surface Processes and Landforms*, *17*(3), 217–234. https://doi.org/10.1002/esp.3290170303

Klinkenberg, Brian. (1994). A review of methods used to determine the fractal dimension of linear features. *Mathematical Geology*, *26*(1), 23–46. https://doi.org/10.1007/BF02065874

Kolzenburg, S., Giordano, D., Thordarson, T., Höskuldsson, A., & Dingwell, D. B. (2017). The rheological evolution of the 2014/2015 eruption at Holuhraun, central Iceland. *Bulletin of Volcanology*, *79*(6), 45. https://doi.org/10.1007/s00445-017-1128-6

Kuntz, M. A., Champion, D. E., Spiker, E. C., Lefebvrelsd, R. H., & Mcbroomes, L. A. (1982).

The Great Rift and the Evolution of the Craters of the Moon Lava Field , Idaho. *Cenezoic Geology of Idaho: Idaho Bureau of Mines and Geology Bulletin*, *26*, 423–437. Retrieved from http://geology.isu.edu/Digital_Geology_Idaho/papers/B-26ch7-2.pdf

Kuntz, M. A., Elsheimer, H. N., Espos, L. F., & Klock, P. R. (1985). *USGS Open-File Report 85-0593: Major-element analyses of latest Pleistocene-Holocene lava fields of the Snake River plain, Idaho*. Retrieved from http://search.ebscohost.com/login.aspx?direct=true&db=geh&AN=1986-014534&site=ehost-live

Kuntz, M. A., Spiker, E. C., Rubin, M., Champion, D. E., & Lefebvre, R. H. (1986). Radiocarbon Studies of Latest Pleistocene and Holocene Lava Flows of the Snake River Plain, Idaho: Data, Lessons, Interpretations. *Quaternary Research*, *25*(02), 163–176. https://doi.org/10.1016/0033-5894(86)90054-2

Kvålseth, T. O. (1985). Cautionary Note about R^2. *American Statistician*, *39*(4), 279–285. https://doi.org/10.1080/00031305.1985.10479448

Leeman, W. P., Vitaliano, C. J., & Prinz, M. (1976). Evolved Lavas from the Snake River Plain. *Contributions to Mineralogy and Petrology*, *56*, 35–60. Retrieved from https://link-springer-com.ezproxy1.library.arizona.edu/content/pdf/10.1007%2FBF00375420.pdf

Li, M., & Li, J. Y. (2017). Generalized Cauchy model of sea level fluctuations with long-range dependence. *Physica A: Statistical Mechanics and Its Applications*, *484*, 309–335. https://doi.org/10.1016/j.physa.2017.04.130

Lifton, N. A., & Chase, C. G. (1992). Tectonic, climatic and lithologic influences on landscape fractal dimension and hypsometry: implications for landscape evolution in the San Gabriel Mountains, California. *Geomorphology*, *5*(1–2), 77–114. https://doi.org/10.1016/0169-555X(92)90059-W

Lipman, P. W., & Banks, N. G. (1987). Aa flow dynamics, Mauna Loa 1984. In R. W. Decker, T. L. Wright, & P. H. Stauffer (Eds.), *Volcanism in Hawaii: U.S. Geological Survey Professional Paper 1350, Volume 2* (pp. 1527–1567). Retrieved from https://www.researchgate.net/publication/262261672

Luongo, G., Mazzarella, A., & Di Donna, G. (2000). Multifractal characterization of Vesuvio lava-flow margins and its implications. *Journal of Volcanology and Geothermal Research*, *101*(3–4), 307–311. https://doi.org/10.1016/S0377-0273(00)00175-X

Macdonald, G. A. (1953). Pahoehoe, aa, and block lava. *American Journal of Science*, *251*(3), 169–191. https://doi.org/10.2475/ajs.251.3.169

Maeno, F., Nakada, S., & Kaneko, T. (2016). Morphological evolution of a new volcanic islet sustained by compound lava flows. *Geology*, *44*(4), 259–262. https://doi.org/10.1130/G37461.1

Mandelbrot, B. (1967). How Long Is the Coast of Britain? Statistical Self-similarity and

Fractional Dimension. *Science (New York, N.Y.)*, *156*(3775), 636–638. https://doi.org/10.1126/science.156.3775.636

Mandelbrot, Benoit B. (1982). *The Fractal Geometry of Nature*. New York: W.H. Freeman. https://doi.org/10.2307/3615422

Mandelbrot, Benoît B. (2002). *Gaussian Self-Affinity and Fractals: Globality, the Earth,1/f Noise, and R/S*. New York: Springer-Verlag.

Maria, A., & Carey, S. (2002). Using fractal analysis to quantitatively characterize the shapes of volcanic particles. *Journal of Geophysical Research: Solid Earth*, *107*(B11), ECV 7-1-ECV 7-17. https://doi.org/10.1029/2001jb000822

Mark, D. M., & Aronson, P. B. (1984). Scale-dependent fractal dimensions of topographic surfaces: An empirical investigation, with applications in geomorphology and computer mapping. *Journal of the International Association for Mathematical Geology*, *16*(7), 671–683. https://doi.org/10.1007/BF01033029

McEwen, A. S., Eliason, E. M., Bergstrom, J. W., Bridges, N. T., Hansen, C. J., Delamere, W. A., et al. (2007). Mars Reconnaissance Orbiter's High Resolution Imaging Science Experiment (HiRISE). *Journal of Geophysical Research*, *112*, E05S02. https://doi.org/10.1029/2005JE002605

Mitchell, N. C., Beier, C., Rosin, P. L., Quartau, R., & Tempera, F. (2008). Lava penetrating water: Submarine lava flows around the coasts of Pico Island, Azores. *Geochemistry, Geophysics, Geosystems*, *9*(3), n/a-n/a. https://doi.org/10.1029/2007GC001725

Moratto, Z., Nefian, A., Beyer, R., Hancher, M., Lundy, M., ALexandrov, O., et al. (2013). *The Ames Stereo Pipeline: NASA's Open Source Automated Stereogrammatry Software*. *Lunar and Planetary Science Conference*. Retrieved from http://hirise.lpl.

Moré, J. J. (1978). The Levenberg-Marquardt algorithm: Implementation and theory. In G. A. Watson (Ed.), *Numerical Analysis* (pp. 105–116). Springer-Verlag. https://doi.org/10.1007/BFb0067700

Neish, C. D., Hamilton, C. W., Hughes, S. S., Nawotniak, S. K., Garry, W. B., Skok, J. R., et al. (2017). Terrestrial analogues for lunar impact melt flows. *Icarus*, *281*, 73–89. https://doi.org/10.1016/j.icarus.2016.08.008

Neuman, S. P., Guadagnini, A., Riva, M., & Siena, M. (2013). Recent Advances in Statistical and Scaling Analysis of Earth and Environmental Variables. In *Advances in Hydrogeology* (pp. 1–25). New York, NY: Springer New York. https://doi.org/10.1007/978-1-4614-6479-2_1

Pedersen, G. B. M., Höskuldsson, A., Dürig, T., Thordarson, T., Jónsdóttir, I., Riishuus, M. S., et al. (2017). Lava field evolution and emplacement dynamics of the 2014–2015 basaltic fissure eruption at Holuhraun, Iceland. *Journal of Volcanology and Geothermal Research*, *340*, 155–169. https://doi.org/10.1016/J.JVOLGEORES.2017.02.027

Peterson, D. W., & Tilling, R. I. (1980). Transition of basaltic lava from pahoehoe to aa, Kilauea Volcano, Hawaii: Field observations and key factors. *Journal of Volcanology and Geothermal Research, 7*(3–4), 271–293. https://doi.org/10.1016/0377-0273(80)90033-5

Pyle, D. M., & Elliott, J. R. (2006). Quantitative morphology, recent evolution, and future activity of the Kameni Islands volcano, Santorini, Greece. *Geosphere*, *2*(5), 253. https://doi.org/10.1130/GES00028.1

Richardson, L. F. (1961). The problem of contiguity: An appendix to "Statistic of Deadly Quarrels." *General Systems: Yearbook of the Society for the Advancement of General Systems Theory, 6*, 139–187. Retrieved from http://cds.cern.ch/record/434833

Rieder, R., Economou, T., Wänke, H., Turkevich, A., Crisp, J., Brückner, J., et al. (1997, December 5). The chemical composition of martian soil and rocks returned by the mobile alpha proton x-ray spectrometer: Preliminary results from the x-ray mode. *Science*. American Association for the Advancement of Science. https://doi.org/10.1126/science.278.5344.1771

Robinson, M. S., Brylow, S. M., Tschimmel, M., Humm, D., Lawrence, S. J., Thomas, P. C., et al. (2010). Lunar Reconnaissance Orbiter Camera (LROC) Instrument Overview. *Space Science Reviews, 150*(1–4), 81–124. https://doi.org/10.1007/s11214-010-9634-2

Rowland, S. K., & Walker, G. P. (1990). Pahoehoe and aa in Hawaii: volumetric flow rate controls the lava structure. *Bulletin of Volcanology*, *52*(8), 615–628. https://doi.org/10.1007/BF00301212

Rowland, S. K., & Walker, G. P. L. (1987). Toothpaste lava: Characteristics and origin of a lava structural type transitional between pahoehoe and aa. *Bulletin of Volcanology*, *49*(4), 631–641. https://doi.org/10.1007/BF01079968

Sandmeyer, E., Nawotniak, S. E. K., Hughes, S. S., Elphic, R. C., Lim, D. S. S., & Heldmann, J. (2017). Frothy Lava At Highway Flow, Craters of the Moon. *Lunar and Planetary Science Conference 48*, #2838.

Schaefer, E. I. (2020). Scale-dependent Fractal Analysis (ver. 0.1). https://doi.org/10.17504/protocols.io.bmm2k48e

Schaefer, E. I., Neish, C. D., Hamilton, C. W., Scheidt, S. P., & Rodriguez Sanchez-Vahamonde, C. D. (2020). The Effects of Sedimentation on the Measured Fractality of Lava Flow Margins. *51st Lunar and Planetary Science Conference*, 2457. Retrieved from https://ui.adsabs.harvard.edu/abs/2020LPI....51.2457S/abstract

Self, S., Thordarson, T., Keszthelyi, L., Walker, G. P. L., Hon, K., Murphy, M. T., et al. (1996). A new model for the emplacement of Columbia River basalts as large, inflated Pahoehoe Lava Flow Fields. *Geophysical Research Letters*, *23*(19), 2689–2692. https://doi.org/10.1029/96GL02450

Self, S., Keszthelyi, L., & Thordarson, T. (1998). The Importance of Pāhoehoe. *Annu. Rev. Earth*

Planet. Sci, *26*, 81–110. https://doi.org/10.1146/annurev.earth.26.1.81

Shean, D. E., Alexandrov, O., Moratto, Z. M., Smith, B. E., Joughin, I. R., Porter, C., & Morin, P. (2016). An automated, open-source pipeline for mass production of digital elevation models (DEMs) from very-high-resolution commercial stereo satellite imagery. *ISPRS Journal of Photogrammetry and Remote Sensing*, *116*, 101–117. https://doi.org/10.1016/j.isprsjprs.2016.03.012

Shenker, O. R. (1994). Fractal geometry is not the geometry of nature. *Studies in History and Philosophy of Science Part A*, *25*(6), 967–981. https://doi.org/10.1016/0039-3681(94)90072-8

Shepard, M. K., Brackett, R. A., & Arvidson, R. E. (1995). Self-affine (fractal) topography: Surface parameterization and radar scattering. *Journal of Geophysical Research*, *100*(E6), 11709. https://doi.org/10.1029/95JE00664

Shepard, M. K., Campbell, B. A., Bulmer, M. H., Farr, T. G., Gaddis, L. R., & Plaut, J. J. (2001). The roughness of natural terrain: a planetary and remote sensing perspective. *Journal of Geophysical Research*, *106*(E12), 32777–32795. https://doi.org/10.1029/2000JE001429

Soule, S. A., & Cashman, K. V. (2005). Shear rate dependence of the pāhoehoe-to-ʻaʻā transition: Analog experiments. *Geology*, *33*(5), 361. https://doi.org/10.1130/G21269.1

Stout, M. Z., Nicholls, J., & Kuntz, M. A. (1994). Petrological and mineralogical variations in 2500-2000 yr B.P. Lava Flows, craters of the moon lava field, idaho. *Journal of Petrology*, *35*(6), 1681–1715. https://doi.org/10.1093/petrology/35.6.1681

Thordarson, T., & Höskuldsson, Á. (2008). Postglacial volcanism in Iceland. *Jökull*, *58*, 197–228.

Thordarson, Thor. (1995). *Volatile release and atmospheric effects of basaltic fissure eruptions*. University of Hawaii, Manoa.

Tolometti, G. D., Neish, C. D., Osinski, G. R., Hughes, S. S., & Kobs Nawotniak, S. E. (2020). Interpretations of Lava Flow Properties from Radar Remote Sensing Data. *Planetary and Space Science*, in review.

Voigt, J. R. C., & Hamilton, C. W. (2018). Investigating the volcanic versus aqueous origin of the surficial deposits in Eastern Elysium Planitia, Mars. *Icarus*, *309*, 389–410. https://doi.org/10.1016/J.ICARUS.2018.03.009

Voigt, J. R. C., Hamilton, C. W., Scheidt, S. P., Steinbrügge, G., Münzer, U., Höskuldsson, Á., et al. (2017). Facies Characterization of the 2014–2015 Holuhraun Lava Flow Field from Remote Sensing Data and Field Observations. *American Geophysical Union Fall Meeting*, P31H-3796. Retrieved from https://ui.adsabs.harvard.edu/abs/2018AGUFM.P31H3796V/abstract

Wolfe, E. W., Neal, C. A., Banks, N. G., & Duggan, T. J. (1988). Geologic observations and

chronology of eruptive events. In E. W. Wolfe (Ed.), *The Puu Oo Eruption of Kilauea Volcano, Hawaii; Episodes 1 Through 20, January 3, 1983, Through June 8, 1984. USGS Professional Paper 1463* (pp. 1–99).

Wroblewski, F. B., Treiman, A. H., Bhiravarasu, S., & Gregg, T. K. P. (2019). Ovda Fluctus, the Festoon Lava Flow on Ovda Regio, Venus: Not Silica-Rich. *Journal of Geophysical Research: Planets*, *124*(8), 2233–2245. https://doi.org/10.1029/2019JE006039

You, J., Kauhanen, K., & Raitala, J. (1996). Fractal properties of outflows from Venusian impact craters. *Earth, Moon and Planets*, *73*(3), 195–214. https://doi.org/10.1007/BF00115880